Far-field speckle correlations as a function of object position for microscopically distinguishing objects hidden in a randomly scattering medium

RYAN L. HASTINGS[1], DAVID W. ALEXANDER[1], AND KEVIN J. WEBB[1,*]

[1] Purdue University, West Lafayette, IN 47907, USA
[*] webb@purdue.cedu

Compiled August 29, 2024

Super-resolution optical sensing is of critical importance in science and technology and has required prior information about an imaging system or obtrusive near-field probing. Additionally, coherent imaging and sensing in heavily scattering media such as biological tissue has been challenging, and practical approaches have either been restricted to measuring the field transmission of a single point source, or to where the medium is thin. We present the concept of far-subwavelength spatial sensing with relative object motion in speckle as a means to coherently sense through heavy scatter. Experimental results demonstrate the ability to distinguish macroscopically identical objects with nanometer-scale translation while hidden in randomly scattering media, without the need for precise or known location and with imprecise replacement. The theory and supportive illustrations presented provide the basis for super-resolution sensing and the possibility of virtually unlimited spatial resolution, including through thick, heavily scattering media with relative motion of an object in a structured field. This work provides enabling opportunities for material inspection, security, and biological sensing.

http://dx.doi.org/10.1364/ao.XX.XXXXXX

1. INTRODUCTION

The motivation for obtaining coherent optical information through randomly scattering media at high resolution is driven by applications as broad as sensing through biological tissue, terrestrial imaging, and condensed matter physics. This has led to investigation of wavefront control [1, 2] and measurement of the field transmission matrix [3] to compensate for the deleterious impact of scatter. There have also been substantial theoretical and numerical investigations of transmission eigenchannels [4, 5], notably drawing upon random matrix theory and related to the eigenvalue density functions [6, 7], motivated in part by studies of Anderson localization [8].

Speckle occurs because of the coherent interaction of waves with random media, and temporal correlations have led to the development of diffuse wave spectroscopy [9] and studies of flow with Brownian motion [10, 11]. Speckle correlations over (as a function of) frequency have allowed studies of interference phenomena [12] and characterization of random media [13]. Spatial and spectral correlations of broadband speckle have also been studied, allowing for applications in non-line-of-sight imaging and imaging of broadband thermal objects [14].

Imaging of an object hidden behind [15] or within [16] a randomly scattering medium has been shown to be possible with measurement of speckle intensity correlations as a function of translated object position. Figure 1(a) illustrates this concept of decorrelating far-field speckle patterns due to the motion of the hidden object. It was thus shown that, with utilization of a theory [17], complex objects could be imaged through thick and very heavily scattering media without the need for characterizing the background properties [18, 19], but with the requirement to estimate or know positional information. Note the minimum in Fig. 1(a) is a measure of the object dimension. Using this general approach, objects were imaged when obscured by corridors of scattering media, including around corners [20]. A detailed theory provides a basis to interpret both macroscopic and microscopic features of the translated hidden object [17]. However, experimental data illustrating sensitivity to the microstructure of an object has been lacking.

The scientific and technological rewards for breaking the link between wavelength and resolution are enormous [21]. Near-field scanning techniques (such as scanning tip microscopy [22]) access the evanescent scattered fields that convey subwavelength spatial information. Near-field speckle has been studied in relation to the microscopic medium elements [23]. Another method makes use of structured illumination and Moiré fringes and grants an increase in resolution by a factor of 2 by extending the range of spatial frequencies that

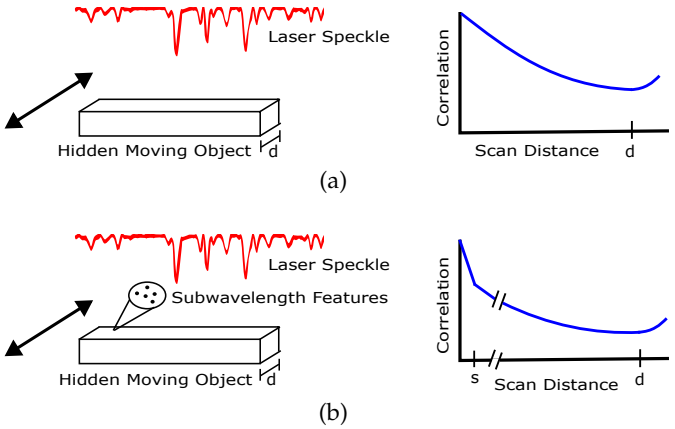

Fig. 1. (a) The concept of relative motion in a speckle field, where a hidden object is translated to a set of positions while intensity speckle pattern are measured by a camera. The speckle pattern decorrelates as the object is scanned. The shape of this curve provides information about the object and, coupled with a theory, a means to image macroscopic objects through heavily scattering media. (b) When an object of interest with small features is translated in a speckle field, these features cause an additional decorrelation in the measured speckle over small length scales. There is no inherent limit to the measurable length scale, implying opportunities for super-resolution sensing. An example is shown of a macroscopic object of width d, with microscopic features represented by s.

can be accessed [24, 25], and this improvement in resolution has been shown to be possible with unknown speckle illumination [26]. While inverting measured data to achieve a resolution far beyond the Abbe limit in the far field generally requires prior information presented as constraints, these have been effectively incorporated. Fluorescence-based techniques such as STED (stimulated emission depletion microscopy), PALM (photoactivated localization microscopy), and STORM (stochastic optical reconstruction microscopy) realize subwavelength resolution [27–29] with use of the point spread function of the microscope as a constraint, and assume a point emitter. These approaches require labeling and provide information about the point location of a fluorophore, but not directly about the underlying geometrical parameters of the sample. The two-fold de Broglie wavelength reduction of entangled photon pairs [30], relative to that for the individual photons, can be, in principle, extended to a larger number of photons. However, the spatial resolution remains that associated with the total energy and hence the parent photon, i.e., again the Abbe resolution. Higher-order photon-counting correlations, in a configuration that extends the Hanbury Brown and Twiss interferometer measurement from two detectors, provide opportunities for higher spatial resolution with statistically independent light sources [31]. Photon correlations to order m have been presented as a means to reduce the width of the point spread function of a microscope by $\sqrt{m}$, offering an avenue for improved spatial resolution [32, 33]. By combining structured illumination with higher-order correlations, further resolution enhancement has been shown for quantum emitters [34]. Finally, accessing spatial mode information has received substantial attention, and axial super-resolution sensitivity using a radial mode sorter has been proposed [35]. While providing important steps, all of these approaches face scaling challenges.

We present experimental results for speckle correlations over translated object position that demonstrate access to geometrical information that in principle can be far-subwavelength. Our understanding is that this is possible because measurements are made at multiple positions with known displacement in a structured illumination (speckle), and the general concept is illustrated in Fig. 1(b). We thus provide an opportunity space, based on relative motion in structured illumination [36] in which far-field intensity measurements facilitate, in principle, resolution of arbitrarily small length scales. This implies sensitivity to far-subwavelength (much smaller than one wavelength) features of objects and distinguishability of objects.

The primary contributions of this work are the experimental results in Sect. 2 that show microstructure information is available that distinguishes objects with speckle correlations over subwavelength distances. An earlier theory that has been used to image translated objects hidden behind thick, heavily scattering media is reviewed in Sect. 3 and projected to provide insight into the experimental results through access to the square of the object function autocorrelation. Using simple examples, Sect. 4 explores how both macroscopic and microscopic features appear in the square of the object function autocorrelation. Some discussion ensues in Sect. 5 and conclusions are drawn in Sect. 6.

2. EXPERIMENTS

We conducted three experiments in which an object of interest was placed between two randomly scattering layers, each composed of three ground-glass slides, and translated over a total distance of approximately two wavelengths. The experimental setup is depicted in Fig. 2 and conforms with that used for imaging hidden macroscopic objects based on speckle correlations over translated object position [18, 19] and the concept of Fig. 1(a). Our goal here is to investigate the degree to which the microstructure of an object can be accessed, as illustrated in Fig. 1(b).

Referring to Fig. 2, the first scattering layer (on the laser side) consisted of two 1500-grit ground glass slides and one 120-grit ground glass slide. The second scattering layer (on the detector side) had three 1500-grit ground glass slides. While the exact scattering properties of these layers are not particularly important, we ensured that each scattering layer had sufficient scatter to produce suitable illumination of the object and fully developed speckle at the detector, as described in Sect. 3. The scattering layers were placed 4 cm apart, with the object of interest located roughly halfway between them. An 850 nm external cavity laser diode (Newport Vortex TLB-6900, 59 mW, 10 MHz linewidth) was used for illumination. The laser beam incident on the first scattering layer was expanded by a lens with a 25 mm focal length to approximately 3.5 cm (vertical) by 1 cm (horizontal) for suitably uniform illumination across the translated object. The object was mounted in a holder attached to a computer-controlled linear stage (Zaber T-LSM150A-S) to move it vertically (with translation step increments that are known). On the camera side, a $4f$ spatial filter was used, with two lenses with 50 mm focal lengths, and an adjustable iris between them. The $4f$ spatial filter regulated the speckle size at the camera to span multiple pixels, allowing adequate resolution of speckle while still allowing approximately ten thousand speckle spots to be imaged [determined from the number of pixels represented by the full width at half maximum of the speckle intensity autocorrelation (25π), the camera array size (1040×1392), and accounting for an equal dark region]. A mag-

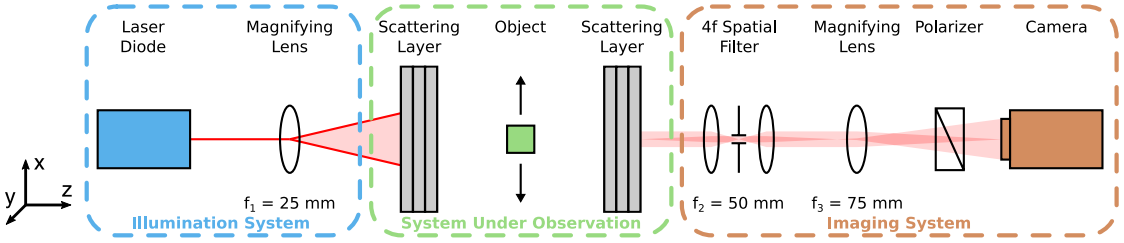

Fig. 2. Diagram of the experimental setup for all the experiments consisting of an 850 nm laser diode (Newport Vortex TLB-6900, 59 mW, 10 MHz linewidth), a magnifying lens ($f_1 = 25$ mm), a ground glass scattering layer, the object of interest, a second ground glass scattering layer, a $4f$ spatial filter containing two lenses ($f_2 = 50$ mm) and an adjustable iris, a second magnifying lens ($f_3 = 75$ mm), a linear polarizer, and a CCD camera (Photometrics Coolsnap HQ). The two scattering slabs are spaced 4 cm apart between their inside faces. The object motion is facilitated by a translational stage (Zaber T-LSM150A-S, 47.6 nm steps).

nifying lens with focal length 75 mm was used to image a small spot on the back of the scattering layer closest to the camera with approximately constant mean intensity, yielding stationary statistics. The camera used was a Photometrics Coolsnap HQ CCD (250 ms integration time). Finally, a linear polarizer was used to ensure zero-mean circular Gaussian field statistics, and hence negative exponential intensity statistics. Speckle images were collected over a known set of translated object positions with vertical displacement, referring to Fig. 2. The images were normalized to yield a mean of zero and a standard deviation of one, with the normalization given by $\tilde{I} = (I - \langle I \rangle)/\sigma_I$, where $\langle I \rangle$ is the mean intensity formed as an average over a given camera image and σ_I is the standard deviation over the camera image. All experiments yielded a contrast ratio close to unity ($\sigma_I / \langle I \rangle \approx 1$).

Fig. 3. Photograph of one of the scattering rods in the experimental setup. The rod is completely obscured from view by the stack of three ground glass slides, and the sample holder is kept out of the beam path.

A motivation behind the setup in Fig. 2 is that the initial randomly scattering layer generates background speckle in which the object of interest is translated. The variable interaction of the translated object with this structured speckle field (where the intensity varies spatially), resulting in changes in the scattered field, presents information about the object's geometry that is encoded in the multiply-scattered field on the camera side (and through the second randomly scattering medium, on the right in Fig. 2) that can be recovered using intensity correlations over object position [17]. From an information theory perspective, information is added by taking multiple measurements at different, known displacements.

Figure 3 shows the obscuring effect of the scattering layers in the experiments described. Interestingly, the character of the random scattering slab on the detector side has an influence on the spatial resolution, and in this way acts as an analyzer, with increased scatter enhancing sensitivity, as previously proposed [37] and investigated using random matrix theory [7] (and as may occur naturally). Specifically, detected information through a scattering analyzer has been shown to result in enhanced spatial sensitivity with motion of an object in a structured field, and that this is accompanied by changes in the relative distribution of significant eigenvalues of the transmission matrix modeling the analyzer [7]. Also, while we present results from the transmission arrangement of Fig. 2, a reflection arrangement is possible.

In the first experiment, the objects of interest were a pair of 6-mm-square scattering rods (clear acrylic with embedded TiO_2 scatterers, 50 nm in diameter, with a reduced scattering coefficient of $\mu_s' = 4$ cm^{-1}), as shown in Fig. 4(a). The experimental arrangement in Fig. 2 was used and the results are shown in Fig. 4(b) and, with an expanded distance scale, in Fig. 4(c). Referring to Fig. 1(b), of interest here and shown in Fig. 4(c) are sample-dependent differences over subwavelength distances and the potential relationship to features on this length scale (s in Fig. 1(b)). It should be noted that a minimum at the object size ($d = 6$ mm, referring to Fig. 1) will only be visible if the scan distance is greater than the size of the object.

Individually, each rod was suspended horizontally and translated vertically (perpendicular to the rod axis) in 47.6 nm steps. Speckle patterns were captured at each rod position, and these were used to form statistical averages for the spatial correlation $\langle \tilde{I}(x_0)\tilde{I}(x_0 + \Delta x)\rangle$, where x_0 is the object's reference vertical position (and with normalized intensities, this becomes unimportant) and Δx is the variable scan distance, which in the experiments totaled just under 2 μm. The spatial correlation at each positional offset, Δx, was formed using all pairs of speckle images sharing this separation [18], resulting in more data samples and hence improved accuracy for the smaller (subwavelength) distances. The experiment was repeated 20 times to provide the average and error bars shown in Fig. 4 ($\pm$ one standard deviation from Gaussian fitting at each Δx). After scanning Rod 1 and then Rod 2 20 times, Rod 1 was placed back into the experiment (with a placement precision better than about 1 mm) and scanned an additional 20 times. The repeatability of the correlation curve corresponding to Rod 1 shows that the significant differences in the curves are due to differences in the rods themselves, rather than experimental error (measurement or placement accuracy). The results in Fig. 4(c) for the two rods show that the curves are distinguishable on a length scale much less than the wavelength, and this indicates subwavelength-scale sensitivity to differences in features of the objects. Both rods were fabricated from the same material and with the same dimensions, making them nominally identical (but of course, they were not). These results, therefore, imply sensitivity to the roughness associated with the rod surfaces and possibly the specific arrangement of the TiO_2 scatterers. Importantly, the

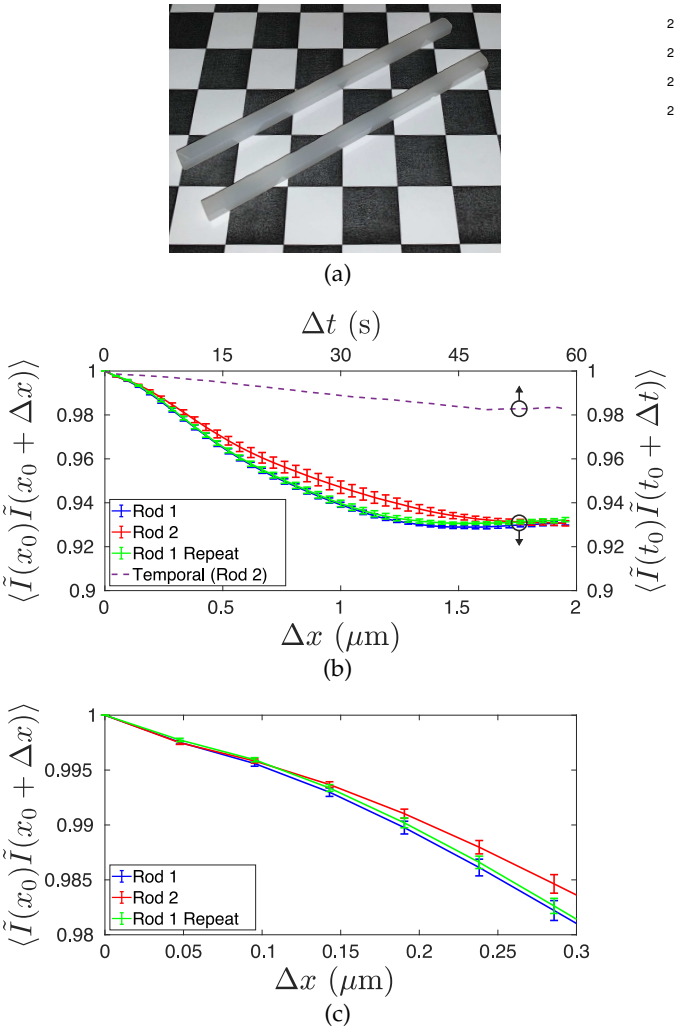

Fig. 4. (a) Photograph of the scattering rods used in the experiments, which were formed from the same slab of acrylic plastic with embedded TiO_2 scatterers, and have the same dimensions of 6 mm $\times$ 6 mm $\times$ 127 mm. (b) Speckle correlations over object position for the two rods, with error bars from 20 data sets. The dotted line shows the measured temporal correlation (over a time similar to that for total number of scans for each rod and hence the duration of the experiment) while the object is held at a single position in the center of the scan. We find this to be negligible, indicating that the decorrelation in the experiment is primarily due to object motion. (c) A magnified plot of the speckle correlations for the rods showing separation (relative to the error bars) at a subwavelength scan distance.

two rods are distinguishable.

In the second experiment, a single rod was scanned 10 times in Orientation 1, then rotated 90 degrees about its long axis and scanned an additional 10 times in Orientation 2, as shown in Fig 5(a). Finally, it was returned to Orientation 1 and scanned 10 times again. The results, presented in Fig. 5(b) and, with an expanded scale over subwavelength distance, in Fig. 5(c), show both sensitivity to the rod orientation and repeatability (with removal and replacement) in the intensity correlation curve with the rod in Orientation 1. These results indicate that if the orientation of the rod is changed, the corresponding intensity correlation curve is different on a subwavelength scale. Consequently, our understanding is that the rotation provides object information along an orthogonal direction, or at least different information about the same object, including microscopic information, consistent with the relevant theory [17].

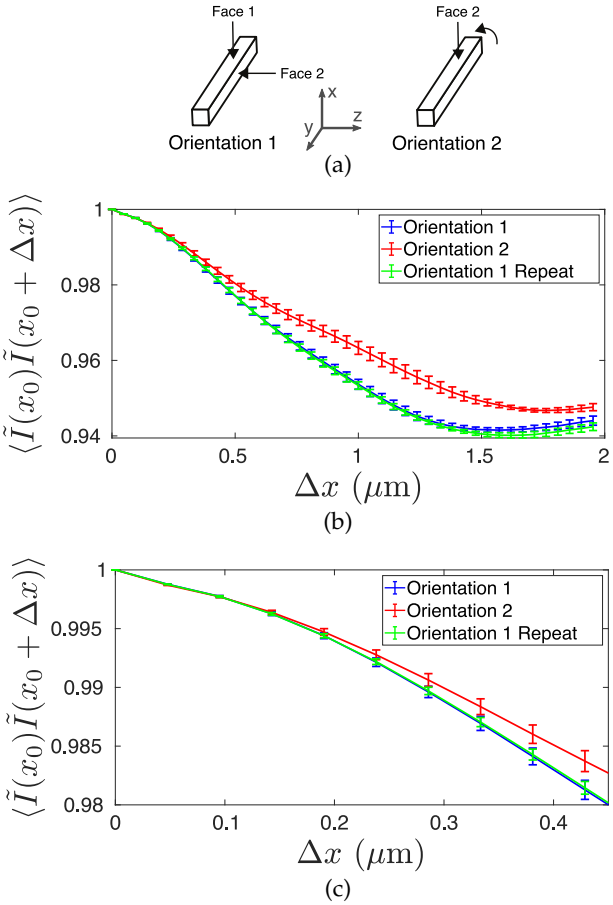

Fig. 5. (a) Diagram showing the 90° rotation of a single scattering acrylic rod, resulting in two orientations. (b) Speckle correlations over object position for the rod in the two orientations, with error bars from 10 data sets. The data indicates that orientation information in relation to the scan direction is available, and also that there is repeatability with removal and imprecise replacement. (c) Rescaled intensity correlation curves show separation of the curves at a subwavelength distance.

In the third experiment, a 1500-grit, 101.6-mm-square ground-glass slide, shown in Fig. 6(a), was translated vertically in 47.6 nm steps while suspended parallel to the scattering layers. After scanning 15 times at Position 1, to form statistical averages, the object was vertically re-positioned by 2 mm to Position 2 and scanned another 15 times. Finally, the slide was placed back at Position 1 and scanned an additional 15 times. The results of this experiment are shown in Fig. 6. Due to differences in surface profile in the two scanned regions of the slide, the intensity correlation curves are distinguishable on a length scale far less than the incident wavelength. With the slide repositioned by 2 mm, the scattered laser light predominantly interacted with features in a different region of the slide, leading to the observed changes in intensity correlation. This experiment indicates that specific local microscopic features of the surface of the ground-glass slide were captured.

Additional experiments were also conducted to measure the effects of temporal decorrelation during the time needed for the

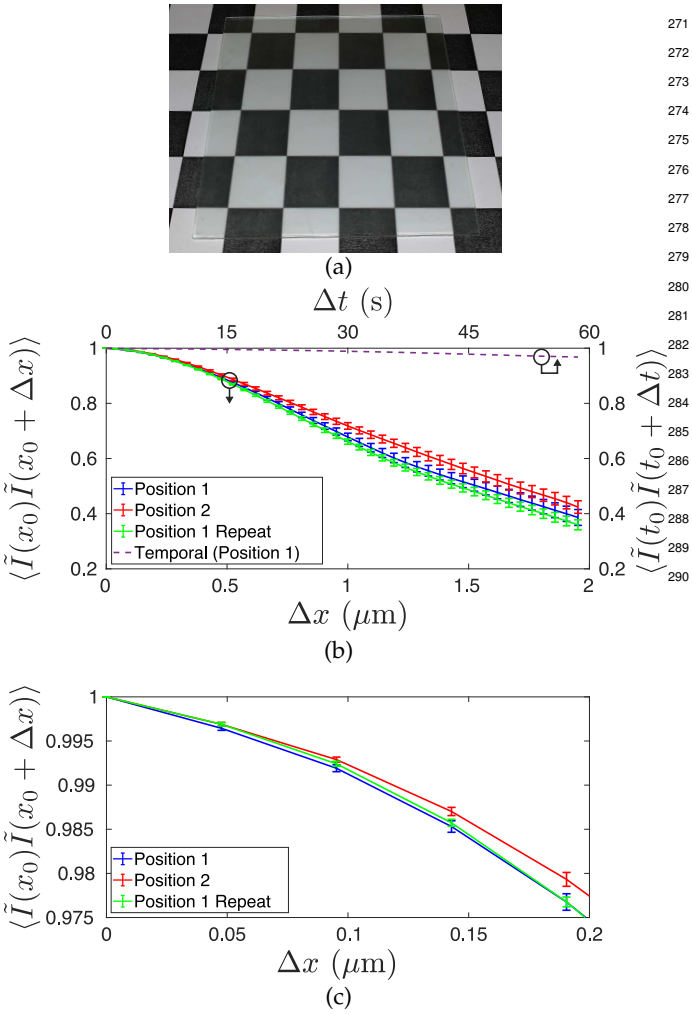

Fig. 6. (a) Photograph of the ground-glass slide used in the experiments. Measured data shows sensitivity to the microscopic surface variations in different regions. (b) Speckle correlations over object position for the ground-glass slide for two different initial positions and error bars from 15 data sets. The separation of the intensity correlation curves at the subwavelength scale is due to differences in surface roughness between the two scanned regions and is indicative of sensitivity to microscopic features. The temporal decorrelation shown, which was obtained over the time taken for the spatially scanned duration of the experiment, is negligible. (c) A magnified plot of the speckle correlations for the slide showing separation at a subwavelength scan distance.

spatial scans for both types of objects. These measurements were carried out by collecting speckle images while keeping the object stationary in the experimental setup. Temporal decorrelation results are shown for the rod experiment in Fig. 4(b) and the ground-glass object case in Fig. 6(b). We found this effect to be negligible compared to the spatial decorrelation, confirming that the behavior of the speckle intensity correlation curves is primarily due to motion of the object relative to the structured field and not temporal instability of the experiment.

3. THEORY

The measured short-range correlations described in Sect. 2 indicate sensitivity to microscopic spatial information from motion in a structured speckled field. This can be understood based on a second-order intensity correlation theory [17], which is reviewed here for completeness and projected in the context of the experimental results of Sect. 2. In this way, an interpretation of the measurements can be made. This theory also forms the basis of some illustrations of the microscopic features available from motion in a structured field that are presented in Sect. 4.

Zero-mean circular Gaussian fields are assumed, consistent with the measurement arrangement in Fig. 2 with a coherent laser and through a linear polarizer. Consequently, we draw upon a moment theorem presented by Reed [38]. The spatial variables are defined in Fig. 7, where the object reference position is $\mathbf{r}_0$, the translation vector is $\Delta\mathbf{r}$, and the single detector point is located at $\mathbf{r}_d$. In the presentation of the experimental results in Sect. 2, a 1D scan was used, so $\mathbf{r}_0 = x_0\,\hat{\mathbf{x}}$ and $\Delta\mathbf{r} = \Delta x\,\hat{\mathbf{x}}$. Mathematically, $\langle\cdot\rangle$ is considered as a configurational average over the background scatterer positions [13, 16] with a single detector point $\mathbf{r}_d$, but in the experiment this is formed from stationary speckle patterns captured at each object position [17], with the intensity normalized as in Sect. 2.

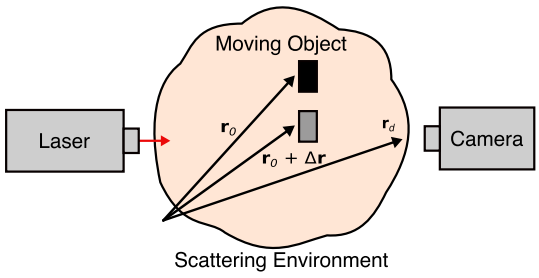

Fig. 7. Geometrical variables for the theory of speckle correlations over the position of a hidden moving object. $\mathbf{r_0}$ and $\mathbf{r_0} + \mathbf{\Delta r}$ are two spatial positions of the moving object, and $\mathbf{r_d}$ is the position of the small spot on the scattering medium onto which the detector is focused.

The vector electric field is sampled through a polarizer, and we describe the resulting scalar field. A decomposition of the total electric field is written as $E(\mathbf{r}) = E_b(\mathbf{r}) + E_s(\mathbf{r})$, where $E_b(\mathbf{r})$ is the field without the translated object of interest, but with all the randomly located scatterers. The additional field resulting from introduction of the scatterer of interest that is translated is given by $E_s(\mathbf{r})$. Such a decomposition is exact [17]. The Helmholtz wave equation can be written with source term corresponding to the dielectric contrast, and this leads to

$$E(\mathbf{r}) \;=\; E_b(\mathbf{r}) + \int O(\mathbf{r}')\;\hat{\mathbf{d}}\cdot\left[\mathbf{G}(\mathbf{r},\mathbf{r}')\mathbf{E}(\mathbf{r}')\right]d\mathbf{r}', \qquad \textbf{(1)}$$

where $O(\mathbf{r}') = -k_0^2\epsilon_s(\mathbf{r}')$, k_0 is the free space wave number ($k_0 = \omega/c$, with ω the circular frequency and c the speed of light in vacuum), $\epsilon_s(\mathbf{r}')$ is the spatially dependent dielectric constant contrast of the moving object of interest (total minus the background), $\hat{\mathbf{d}}$ selects the scalar measured field, and the tensor Green's function $\mathbf{G}(\mathbf{r},\mathbf{r}')$ (the point source response in the temporal frequency domain) is unknown.

At the (equivalent) detector point, $\mathbf{r}_d$, the fourth order field moment can be written in terms of second order moments [38] as

$$\langle I_d(\mathbf{r}_0)I_d(\mathbf{r}_0+\Delta\mathbf{r})\rangle = \langle I_d(\mathbf{r}_0)\rangle\langle I_d(\mathbf{r}_0+\Delta\mathbf{r})\rangle + |\langle E_d^*(\mathbf{r}_0)E_d(\mathbf{r}_0+\Delta\mathbf{r})\rangle|^2. \qquad \textbf{(2)}$$

Using normalized intensities, $\tilde{I} = (I - \langle I \rangle)/\langle I \rangle = (I - \langle I \rangle)/\sigma_I$, where $\langle I \rangle = \sigma_I$ for negative exponential statistics, Eq. (2) becomes

$$\langle \tilde{I}_d(0)\tilde{I}_d(\Delta\mathbf{r})\rangle \quad = \quad \left|\langle \tilde{E}_d^*(0)\tilde{E}_d(\Delta\mathbf{r})\rangle\right|^2. \tag{3}$$

Equation (3) has a consistent field normalization (allowing for non-stationary statistics) that is given by $\tilde{E} = E/\langle I \rangle^{1/2}$, and this renders the absolute reference position $\mathbf{r}_0$ irrelevant (assuming sensitivity requirements are met), leading to the use of $\mathbf{r}_0 = 0$.

The second order field moment at $\mathbf{r}_d$ can be expanded using $E_d = E_{db} + E_{ds}$, as defined in Eq. (1), where E_{db} and E_{ds} are the electric fields at the detector due to the background (all scatterers with the object of interest removed) and the scatterer of interest (the scattered field resulting from insertion of the object), respectively. As detailed in earlier work [17], Eq. (3) can be written as

$$\langle \tilde{I}_d(0)\tilde{I}_d(\Delta\mathbf{r})\rangle = C_0(\Delta\mathbf{r}) + 2\,\mathrm{Re}\left\{C_1^*(\Delta\mathbf{r})g_{ss}^{(1)}(\Delta\mathbf{r})\right\} + C_2(\Delta\mathbf{r})|g_{ss}^{(1)}(\Delta\mathbf{r})|^2, \tag{4}$$

where $\mathrm{Re}\{\cdot\}$ is the real part and the coefficients C_0, C_1, and C_2 are built from rather complicated expressions and depend on translation position in general. The normalized second order field moment in Eq. (4), $g_{ss}^{(1)}$, is given by [17]

$$\begin{aligned} g_{ss}^{(1)}(\Delta\mathbf{r}) &= \langle \tilde{E}_{ds}^*(0)\tilde{E}_{ds}(\Delta\mathbf{r})\rangle \\ &= \int d\mathbf{r}'\tilde{O}^*(\mathbf{r}')\tilde{O}(\mathbf{r}'+\Delta\mathbf{r}), \end{aligned} \tag{5}$$

where the normalized object function, $\tilde{O}(\mathbf{r}')$, is found to survive the averaging process. Equation Eq. (4) with Eq. (5) indicates that speckle correlations over the translated position of a hidden object in randomly scattering media retain information about the object. However, the degrees of freedom in Eq. (4) are not conducive to inversion, where measured data are used to image an object.

Experimental studies with various objects [18, 19] have indicated that C_0 and C_2 could be approximated as constants and that C_1 could be neglected. With these assumptions, Eq. (4) can be simplified as

$$\langle \tilde{I}_d(0)\tilde{I}_d(\Delta\mathbf{r})\rangle = C_0 + C_2|g_{ss}^{(1)}(\Delta\mathbf{r})|^2. \tag{6}$$

Equation Eq. (6) allows experimental data from speckle correlations over translated object position to be used to determine C_0 and C_2. The speckle decorrelation has been found to have a minimum at the object's macroscopic dimension, and this provides C_0 [18]. Subtracting C_0 and then rescaling, we have

$$\langle \tilde{I}_d(0)\tilde{I}_d(\Delta\mathbf{r})\rangle_{\mathrm{sc}} = |g_{ss}^{(1)}(\Delta\mathbf{r})|^2. \tag{7}$$

A Gerchberg-Saxton-type phase retrieval process can be used to image the object and hence obtain $\tilde{O}(\mathbf{r})$, and there are numerous examples of successful macroscopic object imaging [18]. However, our interest here is in the microscopic and potentially subwavelength object information, such as that presented in Sect. 2.

4. MODEL-BASED ILLUSTRATIONS

We now consider some example object functions to explore the relation between a theory that is summarized in Sect. 3 [17] and experimental evidence [16, 18], where the speckle intensity correlation measured as a function of the position of a hidden moving object is predicted to be proportional to the square of the normalized autocorrelation function of the object through Eq. (7) with Eq. (5). Previous experimental work used motion commensurate with the macroscopic (mm-scale) hidden objects that were imaged. Our interest here is in the subwavelength speckle decorrelation in relation to microscopic features on that length scale. Section 2 describes results showing that nominally identical objects with different microscopic features can be distinguished based on intensity correlations over small distances. By considering a macroscopic object with microscopic features, we can understand how speckle intensity correlations can provide access to these two different length scales. To illustrate the possible relationship between the object and the measured speckle, we present some simple examples of how information about small features can be encoded in speckle intensity correlations of larger objects. These examples use the square of the magnitude of the normalized object function autocorrelation (i.e., the predicted result for the speckle intensity correlation from Sect. 3, Eq. (7) with Eq. (5)) for simple macroscopic objects that have differing small-scale features. As the features approach subwavelength size (and hence the speckle size at the object), sensitivity to to small features might reduce, resulting in a practical deviation from this description. However, the experimental results presented in Sect. 2 indicate that distinguishing and characterizing objects from data on that length scale is still possible.

Figure 8 shows a comparison of the expected speckle intensity correlation result for a simple circle having a diameter of 2 arbitrary units (a.u.) with no smaller features, that for a circle of the same diameter with a single weakly scattering smaller feature of diameter 0.05 a.u., and an identical circle with a more heavily scattering small feature. The scattering strength, in this case, refers to the dielectric contrast (ϵ_s), as defined in the object function in Sect. 3. The specific object function values were chosen to illustrate the general trend of the effect on the slope of the correlation curve with relation to the object parameters. The results for the cases with the smaller features show a rapid initial decorrelation from $\Delta x = 0$ until Δx reaches the diameter of the small features. However, all three curves reach a minimum at the diameter of the large circle, showing that both small features and larger features, such as the shape and size of the object, can be seen in the object's autocorrelation function. Additionally, the curve for the circle with the more heavily scattering feature decorrelates more over small Δx, showing sensitivity to scattering strength. Finally, in the autocorrelation curves for the two circles with scattering features, the distances of the edges of the small features to the edges of the circle are seen as changes in the slope of the curves, showing sensitivity to the position of the feature within the circle. This geometrical information is what allows image reconstruction through phase retrieval [18].

Figure 9 shows the expected speckle intensity correlation result for a circle with three small square features, each with the same width of 0.05 a.u., as well as the expected result for an identical structure that has been rotated 90 degrees (i.e., a nominally identical macroscopic object). Again, the diameter of the circle is seen in the minimum of the function, and the size and relative spacing between the various small features are also seen. For instance, both curves experience a rapid initial decorrelation from $\Delta x = 0$ until Δx reaches the diameter of the features, but the two curves begin to separate at $\Delta x = 0.01$ a.u., the smallest edge-to-edge spacing, before the curve for Orientation 1 peaks again slightly at $\Delta x = 0.33$ a.u., the center-to-center spacing in the x-direction of the features. Likewise, the curve

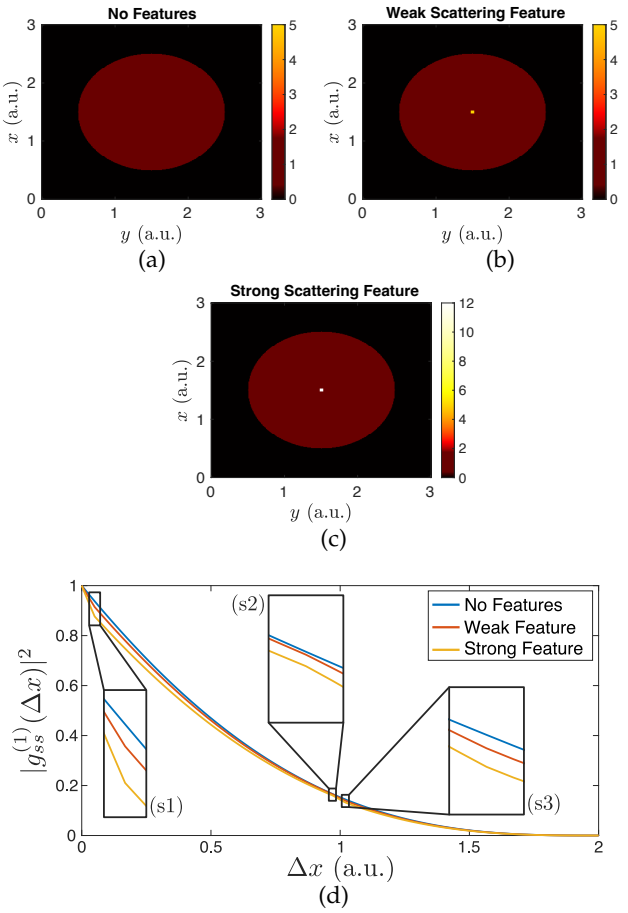

Fig. 8. Effect of a small feature on the modelled speckle intensity correlation result. The values of the circles and smaller features represent differences in dielectric contrast compared to the background: (a) Simple circle of diameter 2 with a uniform value of 1. (b) Circle of diameter 2 (value 1) with a single weakly scattering square scattering feature of diameter 0.05 and value 5. (c) Circle of diameter 2 (value 1) with a single square strongly scattering feature of diameter 0.05 and value 12. (d) Square of the autocorrelation functions as a function of vertical distance, rescaled from 0 to 1, of the three geometries. The curves for the cases with the scattering features show an initial rapid decorrelation from $\Delta x = 0$ to $\Delta x = 0.05$, but behave almost identically to the geometry without the features at larger distances, reaching a minimum at the circle's diameter. Distances between the edges of the feature and the edge of the circle are also seen. (s1) Change in slope at $\Delta x = 0.05$, the diameter of the small feature. (s2) Change in slope at $\Delta x = 0.97$. (s3) Change in slope at $\Delta x = 1.02$. The latter two changes in slope are due to the two edges of the feature being 0.97 and 1.02 away from each edge of the circle.

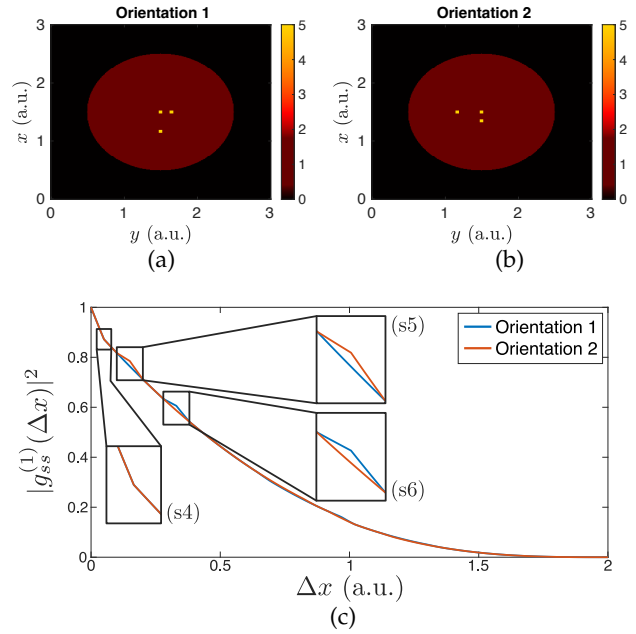

Fig. 9. Geometrical information about small features in modelled speckle intensity correlations. The circles shown have values of 1 and the smaller features have values of 5, representing differences in dielectric contrast. (a) Simple circle with square scattering features of width 0.05, with spacing 0.33 (vertical) and 0.15 (horizontal), center-to-center. (b) An identical object, rotated 90 degrees. (c) Square of the autocorrelation functions of the two circles rescaled from 0 to 1. The two curves separate at $\Delta x = 0.1$, the smallest separation distance between features. (s4) Change in slope at $\Delta x = 0.05$. (s5) Peak at $\Delta x = 0.15$. (s6) Peak at $\Delta x = 0.33$. Distances between the edges of the various features and the edges of the circles are seen as varying changes in slope throughout the curves.

for Orientation 2 shows a small peak at $\Delta x = 0.15$ a.u., the center-to-center spacing between features in the x-direction for that orientation. Small changes in the slope of the curves at Δx values corresponding to distances from the edges of the circles to the edges of the features can also be seen.

Figure 10 compares the expected speckle intensity correlation result of a circle with small rectangular features to that for an identical object which has been rotated 90 degrees. Again, the overall shape and size of the circle is apparent, and the sizes and spacings of the various features are seen in the curves. For example, both curves initially decorrelate rapidly from $\Delta x = 0$ until Δx reaches the diameter of the features in the x-direction. Small peaks are also visible at the center-to-center spacing in the x-direction for each orientation. Small changes in slope are seen at Δx values corresponding to distances from the edges of the circles to the edges of the features. Because the features' orientations change when rotated, the slope of the initial decorrelation changes as well.

The square of an object's autocorrelation function, which is the expected result from Eq. (7) for our speckle intensity correlation experiments for a hidden moving object, contains information about object features of all length scales up to the diameter of the object, including small and potentially subwavelength features. Relevant geometrical features, such as the size and spacing of various small features, are clearly seen in this function for simple objects. For more complex objects, such information is still available, but may be less obvious. However, even for complex objects, distinguishability between macroscopically identical objects could be achievable on an arbitrarily small scale, given sufficient signal-to-noise ratio.

5. DISCUSSION

We can easily see that the object function from motion in structured illumination becomes available for the 1D case and a film (thickness and dielectric constant) [39]. Importantly, now and for the first time, we have insight into the short-range 3D ef-

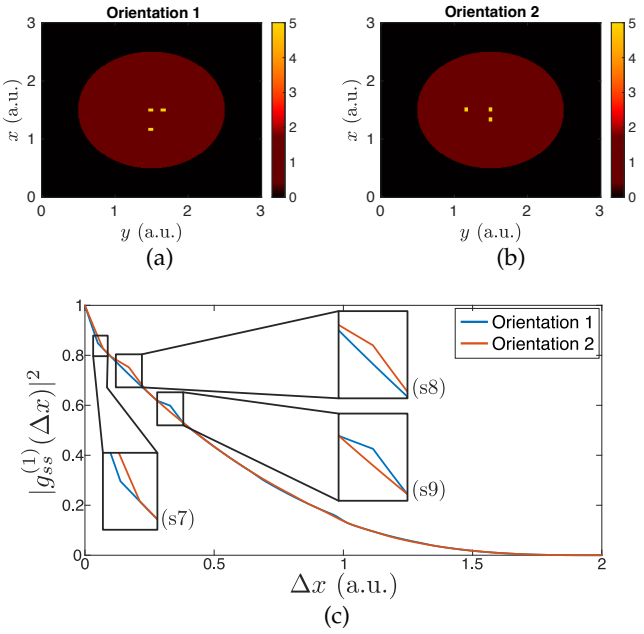

Fig. 10. Separation at small distances in modelled speckle intensity correlation curves caused by small differences in larger scattering features. The circles shown have values of 1 and the smaller features have values of 5, representing differences in dielectric contrast. (a) Simple circle with rectangular scattering features of dimensions 0.05 by 0.07, with spacing 0.33 (vertical) and 0.17 (horizontal), center-to-center. (b) An identical object, rotated 90 degrees. (c) Square of the autocorrelation functions of the two circles (1-dimensional, in the vertical direction), rescaled from 0 to 1. (s7) Changes in slope at Δx = 0.05 and Δx = 0.07, the widths of the features in each orientation. (s8) Peak at Δx = 0.17. (s9) Peak at Δx = 0.33.

fects (small translations relative to the wavelength) in relation to the object geometry from the experimental results in Figs. 4, 5, and 6. Yet to be determined is under what conditions and constraints such data can be inverted to form an image, as was done for macroscopic object functions [18].

Our understanding is that the subwavelength-scale speckle decorrelation has information about object features on this length scale, and that separate macroscopic object information (should this be relevant) results in a decorrelation over a distance corresponding to the spatial support of the object. As an example, if a homogenized object (having a uniform dielectric constant) is scanned, then the minimum of the speckle correlation over position will occur at a distance equal to the object size in that dimension. If we insert small scattering centers (like the 50 nm scatters in the rod experiments of Fig. 4), then there can be an additional subwavelength decorrelation associated with these nanostructures. The propagating plane wave spectrum is influenced by the microstructure; the complete Fourier representation requires the evanescent field portion. With motion in the speckle background, this microstructure information is variably excited in the propagating spectrum, and this can provide a basis for subwavelength information being accessible in the far-field speckle patterns. Earlier theory proposed a joint spatial support argument for deterministic translated object information being available [17]. Here, we show experimental evidence that this can be extended to the microstructure. Illustrations of this concept are shown in Figs. 8 – 10. Earlier, we found that there was an initial decorrelation measured over one wavelength or so that varied for rods of differing material [16]. Now we have results implying that microscopic features can be sensed and characterized with repeatability through speckle correlations in a variety of material systems. Separately, simulations with far-field detection and motion in structured illumination show access to feature separation changes of $\lambda/100$ or smaller [36]. Hence, we know that data conveying geometrical information on nanometer length scales is, in principle, accessible in our experiments. It is through the experimental results described here that we statistically quantify and demonstrate practical utility, implying a new opportunity space for sensing.

An obvious application domain is security labels, motivated by our results showing that two rods can be distinguished (Fig. 4), where we can conceive of constructing unique identifier tags with subwavelength features that cannot be replicated. It also becomes possible to consider inverting such data (at least for simple structures) to form an image on the nanometer length scale using visible light, possibly along the lines of what was done for macroscopic objects [18]. A new material inspection approach based on relative motion, notably of subwavelength defects, becomes feasible along this line. Natural or induced motion could be incorporated into label-free microscopy, offering opportunities in biophysics. We can now conceive of capillary imaging prospects that take diffusing wave spectroscopy (with speckle decorrelation) to a means to image blood constituents rather than simply estimating Brownian motion [9] or flow rate [10]. In a sense, this would be an extension of our previous work involving imaging through several millimeters of tissue [18]. Another opportunity space is the imaging of satellites through a scattering atmosphere, where the scaling of speckle relevant to object features is of interest. Finally, the amount of scatter involved in the experiments suggests additional applications related to sensing of far-subwavelength (or at least higher resolution) features of hidden objects, such as would relate to *in vivo* applications. In this regard, information theoretic studies of scattering matrices would be relevant [40]. There could be opportunities for super-resolution sensing with reduced coherence, and the possibility of resolving two incoherent sources using speckle with a precision not limited by diffraction has been considered theoretically [41]. While there remain some questions about, for instance, the influence of the signal-to-noise ratio in certain scenarios, the results presented here imply sensitivity to microstructure through heavy scatter, fundamental to all of these applications.

6. CONCLUSIONS

The experimental results presented indicate that the specific microscopic features of objects composed of large random arrays of small scatterers can be distinguished in a statistically meaningful sense from average speckle pattern correlations over translated position. This means that information on each or a number of unique scatterer geometries and locations is in principle available in the intensity data from nanometer-scale motion in a speckled field, subject to noise constraints. Earlier work presented a statistical basis for imaging through random media [17] and this was demonstrated for a variety of macroscopic (millimeter-sized) objects [16, 18, 19]. Now we have learned that microstructure information is accessible in a useful manner. Whether inversion of such data to form an image on this length scale is possible remains an open question and will involve suitable measurement diversity and inversion con-

straints. However, the super-resolution potential for this sensing concept alone provides many application opportunities.

FUNDING

Sandia National Laboratories (LDRD); the National Science Foundation Directorate for Engineering (2131486) and Directorate for Computer and Information Science and Engineering (1618908); the Air Force Office of Scientific Research (FA9550-19-1-0067); and a gift from KLA Corporation.

DISCLOSURES

The authors declare no conflicts of interest.

DATA AVAILABILITY

Data is available upon reasonable request.

REFERENCES

1. I. M. Vellekoop and A. P. Mosk, "Universal optimal transmission of light through disordered materials," Phys. Rev. Lett. **101**, 120601 (2008).
2. J. Bertolotti, E. G. van Putten, C. Blum, A. Lagendijk, W. Vos, and A. P. Mosk, "Non-invasive imaging through opaque scattering layers," Nature **491**, 232 – 234 (2012).
3. S. M. Popoff, G. Lerosey, R. Carminati, M. Fink, A. C. Boccara, and S. Gigan, "Measuring the transmission matrix in optics: an approach to the study and control of light propagation in disordered media," Phys. Rev. Lett. **104**, 100601 (2010).
4. K. A. Muttalib, J. L. Pichard, and A. D. Stone, "Random-matrix theory and universal statistics for disordered quantum conductors," Phys. Rev. Lett. **59**, 2475 (1987).
5. Z. Shi and A. Z. Genack, "Transmission eigenvalues and the bare conductance in the crossover to anderson localization," Phys. Rev. Lett. **108**, 043901 (2012).
6. A. Goetschy and A. D. Stone, "Filtering random matrices: the effect of incomplete channel control in multiple scattering," Phys. Rev. Lett. **111**, 063901 (2013).
7. J. A. Patel, Q. Luo, and K. J. Webb, "Eigenchannel analysis of super-resolution far-field sensing with a randomly scattering analyzer," Phys. Rev. A **107**, 023518 (2023).
8. J.-L. Pichard, M. Sanquer, K. Slevin, and P. Debray, "Broken symmetries and localization lengths in anderson insulators: theory and experiment," Phys. Rev. Lett. **65**, 1812 (1990).
9. D. A. Weitz, D. J. Pine, P. N. Pusey, and R. J. A. Tough, "Nondiffusive Brownian motion studied by diffusing-wave spectroscopy," Phys. Rev. Lett. **63**, 1747 (1989).
10. M. Heckmeier, S. E. Skipetrov, G. Maret, and R. Maynard, "Imaging of dynamic heterogeneities in multiple-scattering media," J. Opt. Soc. Am. A **14**, 185–191 (1997).
11. F. Scheffold, W. Härtl, G. Maret, and E. Matijević, "Observation of long-range correlations in temporal intensity fluctuations of light," Phys. Rev. B **56**, 10942–10952 (1997).
12. M. P. van Albada, J. F. de Boer, and A. Lagendijk, "Observation of long-range intensity correlation in the transport of coherent light through a random medium," Phys. Rev. Lett. **64**, 2787–2790 (1990).
13. M. A. Webster, K. J. Webb, and A. M. Weiner, "Temporal response of a random medium from third-order laser speckle frequency correlations," Phys. Rev. Lett. **88**, 033901 (2002).
14. S. Divitt and A. T. Watnik, "Spatial-spectral correlations of broadband speckle in around-the-corner imaging conditions," Opt. Express **30**, 7169–7186 (2022).
15. J. A. Newman and K. J. Webb, "Imaging optical fields through heavily scattering media," Phys. Rev. Lett. **113**, 263903 (2014).
16. J. A. Newman, Q. Luo, and K. J. Webb, "Imaging hidden objects with spatial speckle intensity correlations over object position," Phys. Rev. Lett. **116**, 073902 (2016).
17. K. J. Webb and Q. Luo, "Theory of speckle intensity correlations over object position in a heavily scattering random medium," Phys. Rev. A **101**, 063827 (2020).
18. Q. Luo, J. A. Newman, and K. J. Webb, "Motion-based coherent optical imaging in heavily scattering random media," Opt. Lett. **44**, 2716–2719 (2019).
19. Q. Luo and K. J. Webb, "Parametrization of speckle intensity correlations over object position for coherent sensing and imaging in heavily scattering random media," Phys. Rev. Res. **2**, 033148 (2020).
20. T. Shi, L. Li, H. Cai, X. Zhu, Q. Shi, and N. Zheng, "Computational imaging of moving objects obscured by a random corridor via speckle correlations," Nat. Commun. **13**, 4081 (2022).
21. S. W. Hell, "Far-field optical nanoscopy," Science **316**, 1153–1158 (2007).
22. Y. Inouye and S. Kawata, "Near-field scanning optical microscope with a metallic probe tip," Opt. Lett. **19**, 159–161 (1994).
23. R. Carminati, "Subwavelength spatial correlations in near-field speckle patterns," Phys. Rev. A **81**, 053804 (2010).
24. M. Gustafsson, "Surpassing the lateral resolution limit by a factor of two using structured illumination microscopy," J. Microsc. **198**, 82–87 (2000).
25. R. Heintzmann and C. G. Cremer, "Laterally modulated excitation microscopy: improvement of resolution by using a diffraction grating," Proc. SPIE **3568**, 185–196 (1999).
26. E. Mudry, K. Belkebir, J. Girard, J. Savatier, E. Le Moal, C. Nicoletti, M. Allain, and A. Sentenac, "Structured illumination microscopy using unknown speckle patterns," Nat. Photonics **6**, 312–315 (2012).
27. S. W. Hell and J. Wichmann, "Breaking the diffraction resolution limit by stimulated emission: stimulated-emission-depletion fluorescence microscopy," Opt. Lett. **19**, 780–782 (1994).
28. M. J. Rust, M. Bates, and X. Zhuang, "Sub-diffraction-limit imaging by stochastic optical reconstruction microscopy (storm)," Nat. Methods **3**, 793–796 (2006).
29. E. Betzig, G. Patterson, R. Sougrat, O. Lindwasser, S. Olenych, J. Bonifacino, M. Davidson, J. Lippincott-Schwartz, and H. Hess, "Imaging intracellular fluorescent proteins at nanometer resolution." Science **313**, 1642–1645 (2006).
30. K. Edamatsu, R. Shimizu, and T. Itoh, "Measurement of the photonic de broglie wavelength of entangled photon pairs generated by spontaneous parametric down-conversion," Phys. Rev. Lett. **89**, 213601 (2002).
31. S. Oppel, T. Büttner, P. Kok, and J. von Zanthier, "Superresolving multiphoton interferences with independent light sources," Phys. Rev. Lett. **109**, 233603 (2012).
32. O. Schwartz and D. Oron, "Improved resolution in fluorescence microscopy using quantum correlations," Phys. Rev. A **85**, 033812 (2012).
33. D. Gatto Monticone, K. Katamadze, P. Traina, E. Moreva, J. Forneris, I. Ruo-Berchera, P. Olivero, I. P. Degiovanni, G. Brida, and M. Genovese, "Beating the Abbe diffraction limit in confocal microscopy via nonclassical photon statistics," Phys. Rev. Lett. **113**, 143602 (2014).
34. A. Classen, J. von Zanthier, M. O. Scully, and G. S. Agarwal, "Super-resolution via structured illumination quantum correlation microscopy," Optica **4**, 580–587 (2017).
35. Y. Zhou, J. Yang, J. D. Hassett, S. M. H. Rafsanjani, M. Mirhosseini, A. N. Vamivakas, A. N. Jordan, Z. Shi, and R. W. Boyd, "Quantum-limited estimation of the axial separation of two incoherent point sources," Optica **6**, 534–541 (2019).
36. K. J. Webb, Y. Chen, and T. A. Smith, "Object motion with structured optical illumination as a basis for far-subwavelength resolution," Phys. Rev. Appl. **6**, 024020 (2016).
37. Q. Luo, J. A. Patel, and K. J. Webb, "Super-resolution sensing with a randomly scattering analyzer," Phys. Rev. Res. **3**, L042045 (2021).
38. I. S. Reed, "On a moment theorem for complex Gaussian processes," IRE Trans. Inform. Theory **8**, 194–195 (1962).
39. D. Lin, V. Raghuram, and K. J. Webb, "Determining optical material parameters with motion in structured illumination," Opt. Express **30**, 46010–46019 (2022).

40. D. Bouchet, S. Rotter, and A. P. Mosk, "Maximum information states for coherent scattering measurements," Nat. Phys. **17**, 564–568 (2021).
41. R. Carminati, G. Cwilich, L. S. Froufe-Pérez, and J. J. Sáenz, "Speckle fluctuations resolve the interdistance between incoherent point sources in complex media," Phys. Rev. A **91**, 023807 (2015).